J Mater Sci (2008) 43:4768–4779
DOI 10.1007/s10853-008-2674-2

Size effects in polyurethane bonds: experiments, modelling and parameter identification

Michael Johlitz · Stefan Diebels · Jan Batal · Holger Steeb · Wulff Possart

Received: 13 February 2008 / Accepted: 22 April 2008 / Published online: 20 May 2008

Abstract In this study we examine polyurethane bonds of varying thickness between anodised aluminium substrates. The performed shear tests showed an intriguing size effect of the kind "thinner equals softer". This size effect occurs not only in the basic elasticity (relaxed state), but also in the viscoelastic behaviour of the tested material. The cause of such size effects is supposed to be found in the existence of so-called interphases or boundary layers, which may differ considerably from the bulk in terms of mechanical behaviour, thus having an enormous impact on thin bonds. In thick bonds, however, these interphases or boundary layers have a minor effect on the overall mechanical behaviour. To account for these experimental results in bond modelling, an extended phenomenological continuum mechanics-based model, which explicitly includes such size effects in its calculation, is developed and presented. For this purpose, an abstract structure parameter with its corresponding balance equation is established describing the formation of the interphases by means of a phase transition. This makes it possible to define the bond stiffness at a macroscopic level, without entering into the microstructure. The extended model brings up a set of model parameters, which are determined efficiently by an ES (evolution strategy). The study concludes with a summary and an outlook on our further research work.

M. Johlitz · S. Diebels · J. Batal · H. Steeb (✉) · W. Possart
Saarland University, P.O. Box 11 15 50, 66 041 Saarbrucken, Germany
e-mail: h.steeb@mx.uni-saarland.de

Introduction and motivation

Tests on a variety of epoxy metal and polyurethane metal bond samples have revealed the existence of interphases or boundary layers. Depending on the combination of materials used, these layers are more or less marked and can be detected spectroscopically by calorimetry and also mechanically in the form of size effects [1–11].

The formation of these interphases or boundary layers can be particularly strong in crosslinking systems. The reasons are still not understood in detail, but can be found in several different, even overlapping, mechanisms [6]. At present, there are a number of research programs focusing precisely on this topic (http://www.dfg-spp1369.de).

The size effects showing in the results obtained so far suggest a direct influence of the specific substrate and its surface condition on the adjacent interfacial volume of the crosslinking polymer.

Hence it is essential to explore to which extent a potential interphase or boundary layer affects the practical use of such bonds especially in high-performance applications such as in the automotive and aerospace industries.

Recent publications [12–14] on bond modelling disregard the formation of interphases or boundary layers and their impact on the macroscopic mechanical behaviour of the material compound. Both measurements and simulations still consider the bond as a homogenous, isotropic continuum with hyperelastic mechanical behaviour, without examining interphases or boundary layers. Turning a blind eye on the fact that viscoelasticity is also affected by the interphases or boundary layers, these approaches will remain very limited in describing dynamic loads on the aforesaid bonds.

This is where our study sets in: Polyurethane bonds of varying thickness between anodised aluminium blocks are

shear-tested. The results show a pronounced size effect of the kind "thinner equals softer". This phenomenon is represented by an extended finite viscoelastic material model, the model parameters of which are fitted to the experimental data by evolutionary parameter identification. The model is based upon a scalar structure parameter which satisfies its own balance equation. This structure parameter describes the bond as a transition between two phases, by mediating the properties of a bulk phase material and an interphase or boundary layer material. By coupling the structure parameter's balance equation to the classical momentum balance, both of which are solved as multi-field problems within an inhomogenous finite element analysis, the stiffness variations from the bond interface into the bulk volume can be controlled [15, 16]. Thus it is possible to establish a method to macroscopically detect and model size effects in bonds.

Specimen preparation and shear tests

Sample preparation

AlMg3 is used as raw material for the preparation of the shear samples. The sample blanks (20 mm × 190 mm × 100 mm) (Fig. 1, left) are CNC-machined and provided with the necessary drillings before they are spark-eroded into two point-symmetrical halves (Fig. 1, right). The pairs are numbered to prevent mismatching. The centre surfaces (20 mm × 100 mm) of these paired Al blocks will be used for adhesive bonding after the following surface treatment.

The surfaces are ultrasonically cleaned in acetone for 15 min, etched in 1-molar NaOH for 10 min and pickled in 25% HNO_3 at room temperature, rinsed in distilled water and alcohol and dried. The cleaned halves are then covered with self-adhesive tape, except on the bonding areas (where they need to be anodised), and fastened to the anode of the anodisation unit (Fig. 2) with aluminium screws. Parallel to the bonding surfaces of the samples, a large cathode lies at the bottom of the inner container which is filled with the electrolyte (5% oxalic acid) bathing the samples just above the bonding surfaces.

The inner container is surrounded by another container. The space between both containers is streamed with cold water keeping the anodisation bath temperature always below 40 °C.

The power supply used is able to maintain a maximum current of 25 A at a voltage of 40 V. This is sufficient for simultaneously anodising nine sample halves on the contacted surface area for 2 h.

The following chemical reactions take place during anodisation:

Cathode reaction:

$$6\,H_3O^+ + 6\,e^- \longrightarrow 3H_2 + 6\,H_2O \quad \text{(Reduction)}. \tag{1}$$

Anode reaction:

$$\begin{array}{lll} 1st & : & 2\,Al \longrightarrow 2\,Al^{3+} + 6\,e^- \quad \text{(Oxidation)} \\ 2nd & : & 2\,Al^{3+} + 9\,H_2O \longrightarrow Al_2O_3 + 6\,H_3O^+. \end{array} \tag{2}$$

Total reaction:

$$2\,Al + 3\,H_2O \longrightarrow Al_2O_3 + 3\,H_2. \tag{3}$$

After the anodisation process, the samples are rinsed and kept in distilled water, followed by a two-step ultrasonic cleaning with distilled water and ethanol, whereby the samples are kept for 15 min in each solvent to remove the electrolyte from the pores and make them accessible for the polyurethane during bonding. The ethanol is then removed from the pores by vacuum-drying the samples over night at 120 °C.

Figure 3 shows two views of the anodised surface, as seen by a scanning electron microscope (SEM).

Shear sample bonding: The sample halves are paired according to their numbers and arranged on a clean glass surface (Fig. 2, right). The clearance between the bonding surfaces is adjusted by inserting spacers of predetermined thickness next to the drill holes. Screws are inserted and tightened to preserve the relative position of the two halves.

Prior to bonding, the width of the gap between the paired halves is measured at two opposite positions with

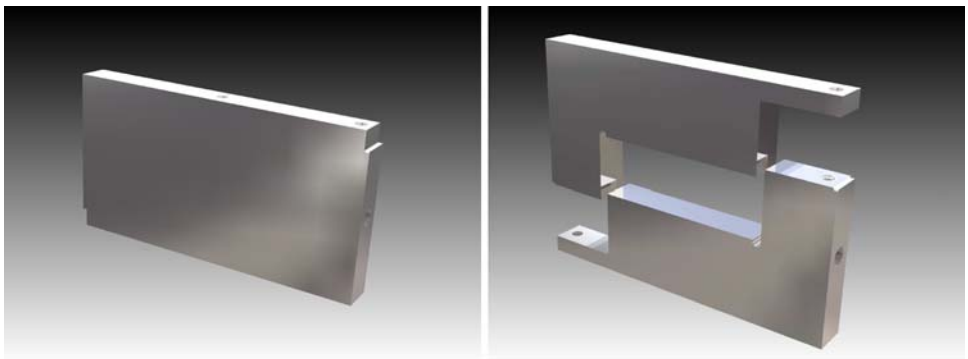

Fig. 1 Blank (left), pair of Al blocks to be bonded (right)

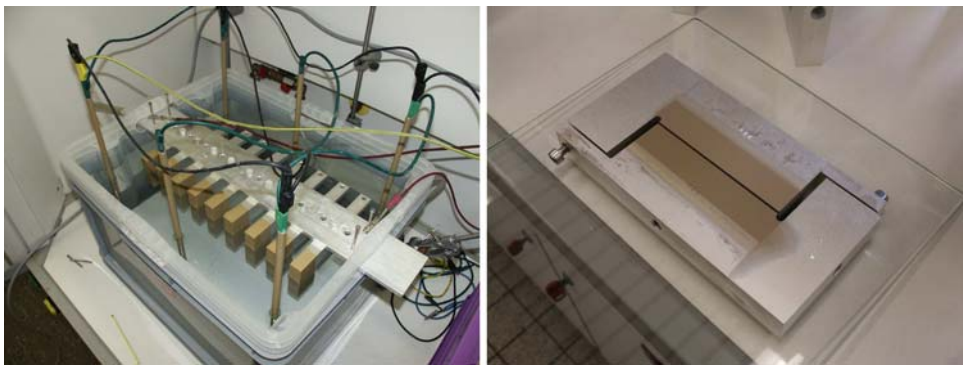

Fig. 2 Anodisation (left), sample ready for bonding (right)

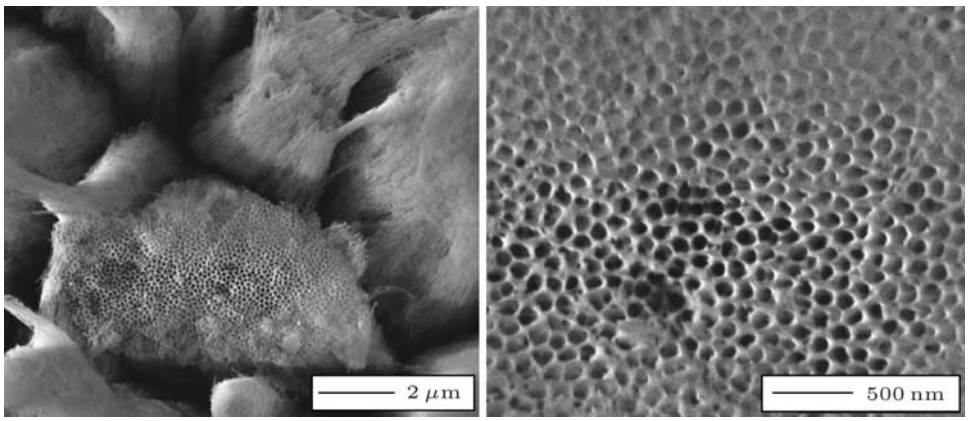

Fig. 3 Pores in the anodised aluminium surface, as seen by a scanning electron microscope

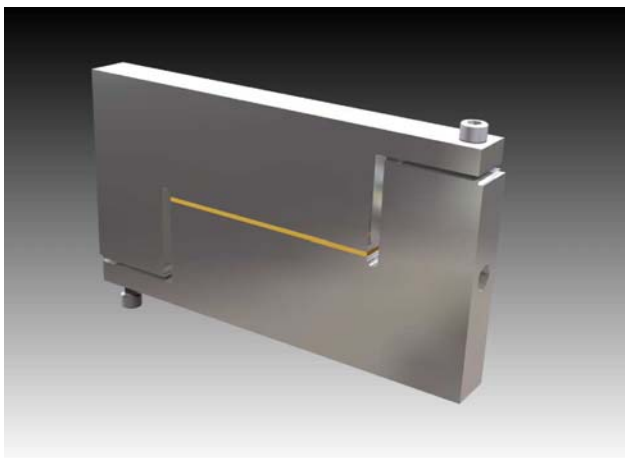

Fig. 4 Adjustment of the clearance between the aluminium blocks and filling the gap with polyurethane

micrometre precision (using a measuring microscope with Quadra-Check). Poor parallelity can be corrected by slightly tightening or loosening one of the screws, if necessary (Fig. 4).

The determined width of the gap is written onto each shear sample.[1] Finally the gap is sealed with self-adhesive tape on the sides and the bottom, leaving it open only on top for later filling with liquid adhesive. The thus prepared samples are introduced into the glovebox, where they are dried in dehumidified air for another night before being finally bonded with the desired polyurethane mixture. This mixture consists of three commercial monomers (isocyanate plus triol plus diol) from Bayer AG. Mixing the triol and diol at a hydroxyl group ratio of 80:20 stoichiometrically with the isocyanate results in a viscoelastic adhesive that is in an entropy elastic state at room temperature and has a glass transition temperature of about 0 °C [17].

The well-stirred, vacuum-degassed, still liquid monomer mix is filled into the gap between the paired halves of the shear samples by means of a pipette. All samples are vacuum-degassed twice in the glovebox transfer port and refilled to make sure that there are absolutely no bubbles left inside the joint. The top side is finally covered with a fully baked-out silicone strip to push away the excessive polyurethane and to give the joint a planar top side with a smooth surface. Figure 4, right, shows a finished polyurethane-filled shear sample.

After six weeks at room temperature in the dehumidified air of the glovebox, the samples are finally annealed for 1 h at 50 °C, and the screws, spacers and silicone strips are removed. This final annealing process is a precaution in order to induce extant Isocyanat-groups to react

[1] The extreme absorptivity of anodised surfaces becomes already obvious at this point: it is not possible to remove the marker ink, not even with acetone.

chemically. After this period of time, one can be sure that the material has reached a stationary condition, and the samples are ready for testing now.

A total of 34 shear samples with bond thicknesses ranging from 80 to 2,200 μm are prepared and tested.

The main advantages of the above method of preparation, based upon the sample geometry, is the precise adjustment and determination of the gap width in the micrometre range as well as the adjustable parallelity (error less than 1.5%) and secure fixation of the gaps during preparation and crosslinking.

High-rate kit (HRK) for GIESA-RS5

The so-called HRK is a self-made measuring add-on for the commercial shearing machine RS5 by GIESA mbH, Wilsdraff, Germany. The RS5 has a maximum sampling rate of 1 Hz only, which is insufficient for tests even with moderate shear rates, let alone higher ones. The HRK is tailored to the special sample geometry (see section Sample Preparation) and has its own force sensor (10 kN@1 N, mounted with an adapter on top of the sample) and displacement sensor (3 mm@ 2 μm, attached directly to the sample with two brackets) (Fig. 5), which allow sampling rates of up to 1 kHz. The RS5's own sensors are not in use during the measurements.

Experiments and analysis

The following shear tests are performed, assuming that the bond thickness does not change during testing:

- Cyclic testing for preconditioning of the samples
- Quasi-static testing to determine the elastic behaviour
- Testing at different shear rates to determine the viscoelastic behaviour

Previous tests showed no linear correlation between the machine speed set on the RS5 and the actual shear rate applied to the samples. This is no surprise, as different bond thicknesses oppose more or less resistance to the machine stiffness of the RS5. By measuring the relative displacement directly on the paired blocks, it is possible to relate the machine speeds to the desired shear rates of samples with determined bond thicknesses.

With maximum machine speed, it is possible to cover three decades (between 0.00004 and 0.04 s^{-1}) of shear rates for all bond thicknesses.

For preconditioning, the samples were loaded cyclically with a shear rate of 0.004 s^{-1} in the examined deformation range of 0.5, i.e., a shearing angle of 26.6°. No stiffness reduction (Mullins effect) could be observed after the first cycles (Fig. 6), which is plausible for an unfilled, fully

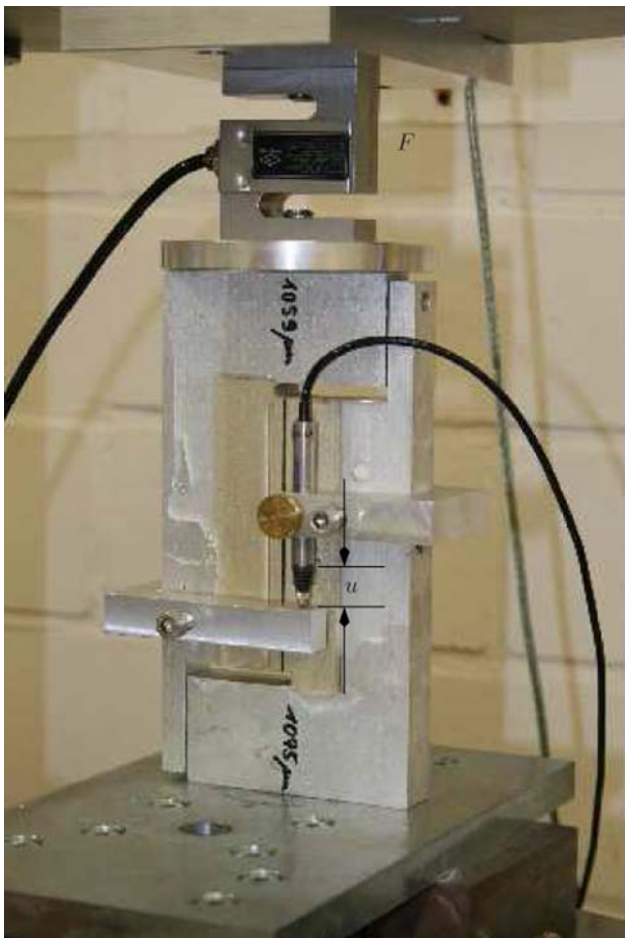

Fig. 5 GIESA RS5 with High-Rate Kit installed

cured adhesive. Thus preconditioning could be limited to 3 cycles before testing each sample.

The cyclic tests reveal a pronounced size effect of the kind "thinner equals softer". This effect is perceivable in both basic elasticity and viscoelasticity. The size effect in basic elasticity can easily be observed in the different slopes of the stress/shear lines. The size effect in viscoelasticity can be seen in the different areas of the hysteresis loops, which, at constant shear rates, depend on the bond thickness (Fig. 6). The exact correlation is analysed in detail below.

The two smallest shear rates (0.00004 and 0.0004 s^{-1}) yielded identical results without hysteresis. This means that no rate-dependent behaviour was activated by the rate 0.0004 s^{-1}. In order to save testing time, this rate was used for quasi-static testing. Figure 7 shows the effective shear moduli of the basic elasticity of all samples as a function of bond thickness. The plateau on the right side of the graph shows the bulk value of $\mu_{\text{eff}} = 1.70$ MPa. The curvature of the graph increases below a bond thickness of about 500 μm, thus clearly indicating a size effect of the kind "thinner equals softer".

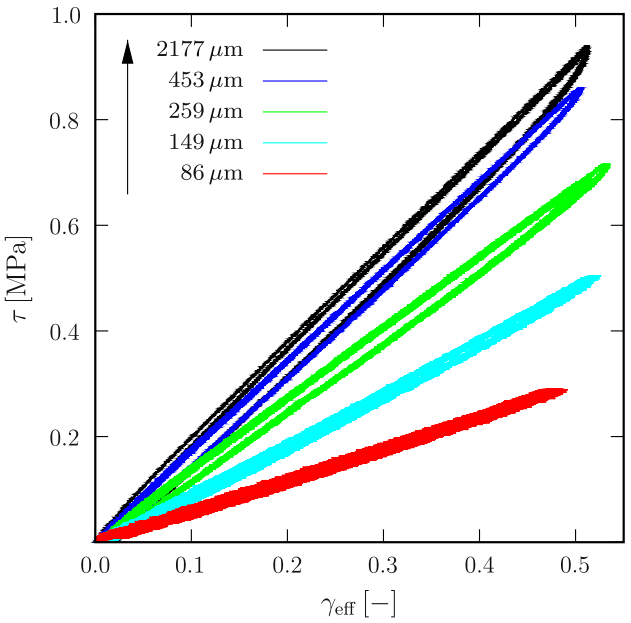

Fig. 6 Cyclic testing with 0.004 s^{-1} on different bonds. The curves of the first cycles are always retraced by the following cycles

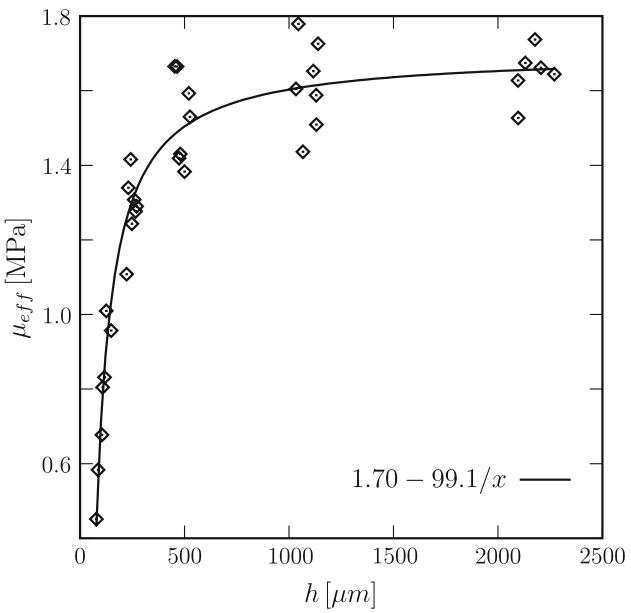

Fig. 7 Effective shear moduli as a function of bond thickness with mathematical, non-linear regression

To facilitate a later identification of material parameters within the extended model, a non-linear, hyperbolic regression is used to approximate the data:

$$\mu_{\text{eff}} = 1.70\,\text{MPa}\left(1 - \frac{99.1\,\mu\text{m}}{1.70\,h}\right). \quad (4)$$

This function is the best result obtained with a commercial data analysis tool (Table Curve).

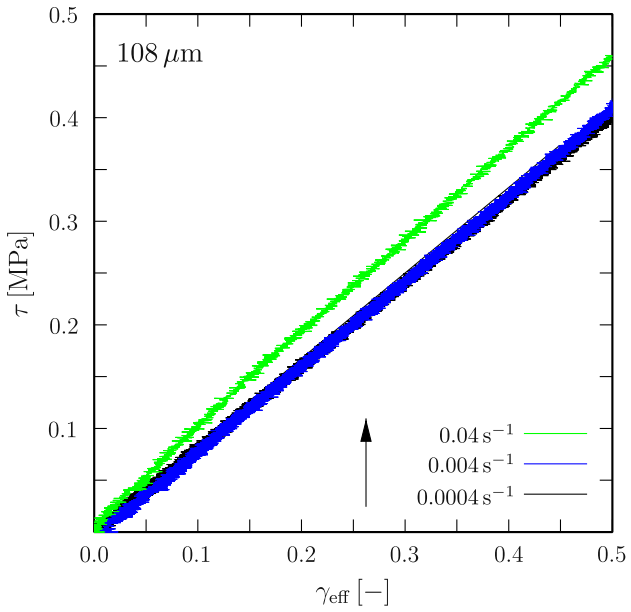

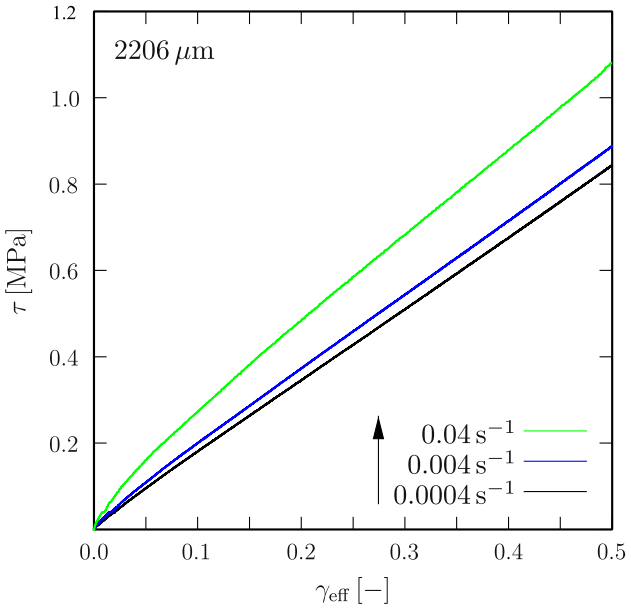

Fig. 8 Experimental results for bonds with different thicknesses sheared at constant rates of 0.0004 (basic elasticity), 0.004 and 0.04 s^{-1}

Experiments with constant shear rates

For analysis of the shearing samples' mechanical behaviour, one has to consider that the desired deformation rate does not settle until after a short acceleration period of the RS5. This non-linear part is accounted for in the simulation as a non-linear time-dependent Dirichlet boundary condition. This non-linearity increases with higher rates of deformation.

The graphs in Fig. 8 show examples for the shear stress τ plotted against the shear deformation $\gamma_{\text{eff}} = u/h$ of bonds

with different thicknesses. The deformation behaviour is analysed over two decades of shear rates ranging from 0.0004 s^{-1} (basic elasticity) to 0.004 s^{-1} and up to 0.04 s^{-1}. Qualitatively one can observe the same kind of rate dependency for different bonding thicknesses. Furthermore, the two rates that activate viscoelasticity were examined (Fig. 9). For that purpose, the effective total stress $\tau = \tau_{eq} + \tau_{neq}$ is plotted against the effective shear γ_{eff} for every bond thickness. Here one can see that, in addition to the size effect depending on the bond thickness, there is a linear coincidence between the two shear rates. To determine the relaxation behaviour, different shear levels were approached, the machine was stopped and the stress relaxation was recorded over time. It must be clearly stated that this is not a pure relaxation test, as the state of deformation cannot be kinematically fixed and the sample partially eludes the force of the machine. It is rather a mix of relaxation and retardation test. Hence it will not be given further consideration here.

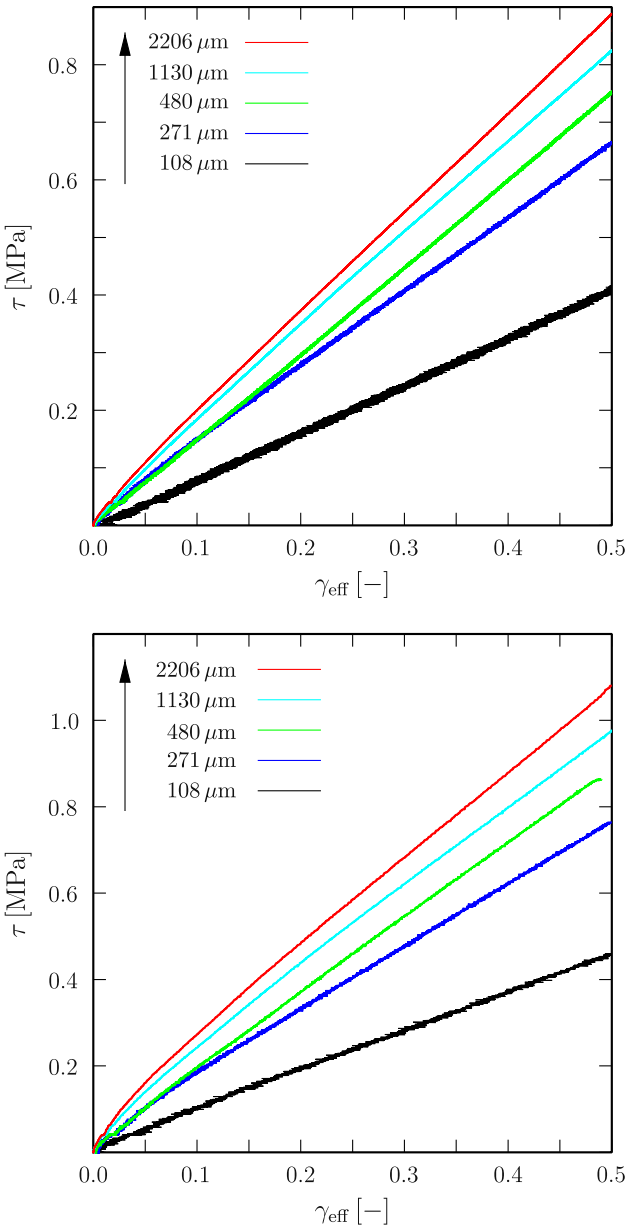

Fig. 9 Experimental results for bonds with different thicknesses sheared at constant rates of 0.004 s^{-1} (up) and 0.04 s^{-1} (down)

The experimental results are rather challenging for theoretical modelling and identification of parameters. These aspects will be discussed in the next section.

Modelling aspects and parameter identification

Theoretical modelling

In this section we present a new extended phenomenological continuum mechanics-based model, which is able to adequately reflect the results observed in the experiments by means of a finite viscoelastic material description. Subsequently, the required basic theory will be derived and documented, whereby isothermal conditions and quasi-static processes (i.e., disregard of inertia terms) are assumed and long-range effects are neglected.

At this point, a non-dimensional, abstract structure parameter $\kappa(\mathbf{x}, t)$ is introduced. This parameter κ is an additional degree of freedom and allows to formally model the assembling of a bond in the sense of a phase transition, i.e. κ describes a continuous transition from a "bulk material" to an "interphase material". The structure parameter does not dispose of an evolution equation but on a field equation for which associated boundary values can be prescribed. Hence, the existence of interphases/boundary layers can be controlled by the boundary conditions of this parameter. Disregarding long-range effects, assuming isothermal and quasi-static conditions, the balance equation for the structure parameter κ is introduced [15, 18] as

$$\operatorname{div} \mathbf{S} + \hat{\kappa} = 0, \tag{5}$$

comparable to the balance of equilibrated forces [19] where $\mathbf{S}$ describes the vector-valued flux of κ and $\hat{\kappa}$ represents a production term. κ itself is to be determined numerically as part of a boundary value problem and can take values between 0 and 1. For the primary variable κ, Dirichlet boundary conditions can be specified. In a physical sense, this structure parameter describes a phase transition between an interphase or boundary layer ($\kappa := 1$) and the bulk phase ($\kappa := 0$) [20, 21]. Equation 5 can be derived by an extended energy balance, as it can be found in the works of Capriz [22, 23], Svendsen [24, 25] and Steeb et al. [18]. Comparing the procedure presented here to the invariance evaluation of the extended energy balance, it is obvious

that $\hat{\kappa}$ does not contribute to energy. Furthermore the classical momentum balance

$$\text{div } \mathbf{T} = \mathbf{0}, \tag{6}$$

is introduced, where the tensor $\mathbf{T}$ describes the Cauchy stress. Both Eqs. 5 and 6 have to be completed by constitutive equations for $\mathbf{S}$, $\hat{\kappa}$ and $\mathbf{T}$.

For the reason that our model works in the frame of the finite viscoelasticity, we have to introduce and resume the theory shortly. There are many publications in the field of finite viscoelasticity dealing with thermomechanical modelling of rubber-like, quasi-incompressible materials, the interested reader is referred to e. g. Coleman et al. [26, 27], Chadwick [28], Alts [29], Haupt [30–32], Göktepe et al. [33–36], Keck [37], Reese [38], Reese and Govindjee [39, 40], Reese and Wriggers [41, 42], Lion [43–46], Sedlan [47], Amin [48–50], Laiarinandrisana [51], Boyce et al. [52–56], Besdo et al. [57, 58], Ihlemann [59].

The formulation of finite viscoelasticity in our work originates from the concept of deformation-valued internal variables. The theory presented is mainly based upon the work of Lion [43–46], Sedlan [47], Reese et al. [41], Lubliner [60] and Le Tallec [61].

The starting point of our continuum-mechanical considerations is a rheological model, in which a spring is connected in paralleled with $j = 1,\ldots,n$ spring dashpots, the so-called Maxwell elements. While the single spring stands for the basic elasticity of the material, the Maxwell elements are able to represent viscoelastic material behaviour of any complexity level.

In order to describe the experimental results in terms of continuum mechanics within the framework of a finite theory, we start with a multiplicative split of the deformation gradient $\mathbf{F}$ into an elastic part $\mathbf{F}_e^j$ and an inelastic part $\mathbf{F}_i^j$. $\mathbf{F}_e^j$ describes the elastic deformation in the j-th Maxwell element and $\mathbf{F}_i^j$ describes the inelastic deformation, respectively. With respect to Fig. 10, $\mathbf{F}_e^j$ is a measure for the elongation of the spring with stiffness μ_e^j while $\mathbf{F}_i^j$ represents the elongation of the dashpot with its relaxation time r^j. This assumption is purely constitutive. This multiplicative split of the deformation gradient and the related

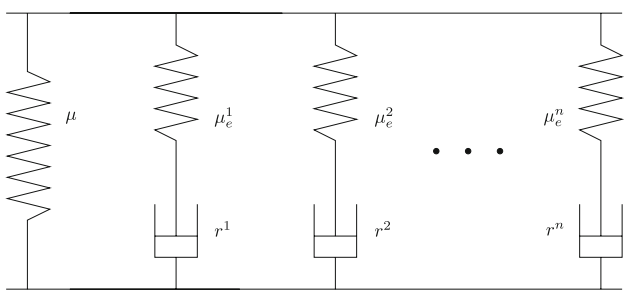

Fig. 10 Rheological model of viscoelasticity with $j = 1 \ldots n$ Maxwell elements. Each spring element is of non-linear Neo–Hooke-type

concepts were first introduced in crystal plasticity [62–64]. For every Maxwell element, a fictitious intermediate configuration is introduced, where the finite strain tensor living on this configuration is divided additively into an elastic part and an inelastic part so that the theory of the rheological model (additive split of the deformation) can be applied with respect to finite deformation.

The deformation tensors of the resulting deformation and stress magnitudes in their corresponding reference, intermediate and current configuration will now be presented briefly. The inelastic, right Cauchy-Green deformation tensors $\mathbf{C}_i^j := \mathbf{F}_i^{jT} \cdot \mathbf{F}_i^j$ describe the inelastic deformation of the dashpots in the reference configuration, while the elastic, left Cauchy-Green deformation tensors $\mathbf{B}_e^j := \mathbf{F}_e^j \cdot \mathbf{F}_e^{jT}$ describe the springs within the Maxwell elements in the current configuration. The correlation between the deformation tensors $\mathbf{C}_i^j$ and $\mathbf{B}_e^j$ is as follows:

$$\mathbf{B}_e^j = \mathbf{F} \cdot (\mathbf{C}_i^j)^{-1} \cdot \mathbf{F}^T. \tag{7}$$

The second order tensors $\mathbf{C}_i^j$ are treated as internal variables and their evolution will be prescribed constitutively.

The required constitutive equations have to be formulated in a thermomechanical consistent framework. Therefore, the entropy balance in form of the Clausius–Planck inequality is evaluated. Hence, the specific free Helmholtz energy Ψ is defined in the form of the Legendre transformation. Before setting up the free Helmholtz energy function and evaluating the entropy balance, the process variables

$$\mathcal{S} = \left\{\mathbf{B}, \mathbf{B}_e^j, \kappa, \ \text{grad } \kappa\right\}, \tag{8}$$

are chosen. The response functions $\mathcal{R} = \{\Psi, \mathbf{T}, \mathbf{S}, \hat{\kappa}\}$ are assumed to depend explicitly on $\mathcal{S}$ only. The free Helmholtz energy function is constitutively split into an equilibrium part and n non-equilibrium parts. The equilibrium part describes the basic elasticity, while the non-equilibrium parts describe the time-dependent viscoelastic material behaviour. Additionally the free energy function is split into a bulk part Ψ^{B} and an interphase part Ψ^{I}. The split of the free energy function reads in detail:

$$\begin{aligned}\Psi = &\Psi^{\mathrm{B}}_{eq}(\mathrm{I}_{\mathbf{B}}, \kappa) + \Psi^{\mathrm{I}}_{eq}(\mathrm{I}_{\mathbf{B}}, \kappa) \\ &+ \sum_{j=1}^{n} \Psi^{\mathrm{B}}_{neq}(\mathrm{I}_{\mathbf{B}_e^j}, \kappa) + \sum_{j=1}^{n} \Psi^{\mathrm{I}}_{neq}(\mathrm{I}_{\mathbf{B}_e^j}, \kappa) \\ &+ \Psi^{\mathrm{S}}(\kappa, \ \text{grad } \kappa).\end{aligned} \tag{9}$$

Only the dependence of Ψ on the first invariants $\mathrm{I}_{\mathbf{B}}, \mathrm{I}_{\mathbf{B}_e^j}$ of $\mathbf{B}$ and $\mathbf{B}_e^j$, respectively, is taken into account. As will be seen later a possible dependence on the second invariant $\mathrm{II}_{\mathbf{B}}$ is not required to represent the measured data. Thus, coupling terms are assumed between the first invariant $\mathrm{I}_{\mathbf{B}}$ of the left Cauchy-Green deformation tensor $\mathbf{B}$ and the structure parameter κ in

both elastic (basic elasticity) and inelastic behaviour (viscoelasticity). As a constitutive law, an approach of the Neo–Hooke [65, 66] type is obtained elastic (basic elasticity) and inelastic behaviour (viscoelasticity).

Choosing the process variables $\mathcal{S}$ and following the standard evaluation of the entropy principle yield the following inequality

$$\left(\mathbf{T}+p\mathbf{I}-2\mathbf{B}\cdot\frac{\partial\Psi^{\mathrm{B,I}}_{eq}}{\partial\mathbf{B}}-\sum_{j=1}^{n}2\,\mathbf{B}^{j}_{e}\cdot\frac{\partial\Psi^{\mathrm{B,I}}_{neq}}{\partial\mathbf{B}^{j}_{e}}\right):\mathbf{D}+\left(\mathbf{S}-\frac{\partial\Psi}{\partial\ \mathrm{grad}\ \kappa}\right)\cdot(\mathrm{grad}\,\kappa)^{\cdot}+\left(-\widehat{\kappa}-\frac{\partial\Psi}{\partial\kappa}\right)\dot{\kappa}-\sum_{j=1}^{n}\frac{\partial\Psi^{\mathrm{B,I}}_{neq}}{\mathbf{C}^{j}_{i}}:\dot{\mathbf{C}}^{j}_{i}\geq 0. \tag{10}$$

In this connexion $\mathbf{D}$ is the rate of the deformation tensor with respect to the current configuration. The incompressibility condition $\mathrm{div}\dot{\mathbf{x}}=\mathbf{I}:\mathbf{D}=0$ was added to the entropy inequality in combination with a Lagrange multiplier p. The second-order tensor $\mathbf{I}$ is the identity tensor.

The evaluation of the entropy principle concerning the argumentation of Coleman and Noll [26] yields the following set of constitutive equations for the Cauchy stress $\mathbf{T}$,

$$\mathbf{T}=-p\mathbf{I}+2\mathbf{B}\cdot\frac{\partial\Psi^{\mathrm{B,I}}_{eq}}{\partial\mathbf{B}}+\sum_{j=1}^{n}2\,\mathbf{B}^{j}_{e}\cdot\frac{\partial\Psi^{\mathrm{B,I}}_{neq}}{\partial\mathbf{B}^{j}_{e}}, \tag{11}$$

for the vector-valued flux term $\mathbf{S}$ according to the structure parameter κ,

$$\mathbf{S}=\frac{\partial\Psi}{\partial\mathrm{grad}\ \kappa}, \tag{12}$$

and at least for the production term $\hat{\kappa}$

$$-\widehat{\kappa}=\frac{\partial\Psi}{\partial\kappa}. \tag{13}$$

As a constitutive law, an approach of the Neo–Hooke [65, 66] type is obtained for both the single non-linear spring and the n springs within the Maxwell elements, as it is able to accurately describe the behaviour observed. In detail, the bulk phase part and the interphase part of the free energy, Ψ^{B} and Ψ^{I}, respectively, are as follows:

$$\begin{aligned}
&\Psi^{\mathrm{B}}_{\mathrm{eq}}(\mathrm{I}_{\mathbf{B}},\kappa)=(1-\kappa)\,\frac{1}{2}\,\mu_{\mathrm{B}}\,(\mathrm{I}_{\mathbf{B}}-3),\\
&\Psi^{\mathrm{I}}_{\mathrm{eq}}(\mathrm{I}_{\mathbf{B}},\kappa)=\kappa\,\frac{1}{2}\,\mu_{\mathrm{I}}\,(\mathrm{I}_{\mathbf{B}}-3),\\
&\sum_{j=1}^{n}\Psi^{\mathrm{B}}_{\mathrm{neq}}(\mathrm{I}_{\mathbf{B}^{j}_{e}},\kappa)=\sum_{j=1}^{n}(1-\kappa)\,\frac{1}{2}\mu^{j}_{\mathrm{B}}(\mathrm{I}_{\mathbf{B}^{j}_{e}}-3),\\
&\sum_{j=1}^{n}\Psi^{\mathrm{I}}_{\mathrm{neq}}(\mathrm{I}_{\mathbf{B}^{j}_{e}},\kappa)=\sum_{j=1}^{n}\kappa\,\frac{1}{2}\mu^{j}_{\mathrm{I}}(\mathrm{I}_{\mathbf{B}^{j}_{e}}-3),\\
&\Psi^{\mathrm{S}}(\kappa,\ \mathrm{grad}\ \kappa)=\alpha\,\kappa^{2}+\beta\,(\mathrm{grad}\ \kappa)^{2}.
\end{aligned} \tag{14}$$

For the phase transition part, a square term in κ and its gradient grad κ forms the basis. This is the easiest ansatz one can define. As will be shown, the chosen ansatz fits the experimental data very well. Another motivation for Ψ^{S} can be found for example in Cahn and Hilliard [67]. Therein, a similar ansatz Ψ^{S} is chosen in order to model a phase field. In this context κ describes the interface energy while grad κ is responsible for the interface's thickness. The model parameters are the shear modulus of basic bulk elasticity μ_{B}, the shear modulus of basic interphase elasticity μ_{I} and the shear moduli of the corresponding springs within the n Maxwell elements of both the bulk phase μ^{j}_{B} and the interphase μ^{j}_{I}. α and β are further model parameters governing the phase transition from the bulk to the interphase material. Evaluating the Clausius–Planck inequality according to the Eqs. 10–13, we obtain the constitutive equation of the Cauchy stress tensor

$$\mathbf{T}=-p\mathbf{I}+[(1-\kappa)\mu_{\mathrm{B}}+\kappa\mu_{\mathrm{I}}]\mathbf{B}+\sum_{j=1}^{n}\left[(1-\kappa)\mu^{j}_{\mathrm{B}}+\kappa\mu^{j}_{\mathrm{I}}\right]\mathbf{B}^{j}_{e}, \tag{15}$$

which is split into equilibrium stresses and non-equilibrium stresses, an equation for the vector-valued flux

$$\mathbf{S}=\beta\,\mathrm{grad}\,\kappa, \tag{16}$$

and the production term of κ

$$\hat{\kappa}=-\left[\alpha\kappa+\frac{1}{2}(\mu_{\mathrm{I}}-\mu_{\mathrm{B}})(\mathrm{I}_{\mathbf{B}}-3)+\sum_{j=1}^{n}\frac{1}{2}\left(\mu^{j}_{\mathrm{I}}-\mu^{j}_{\mathrm{B}}\right)(\mathrm{I}_{\mathbf{B}^{j}_{e}}-3)\right]. \tag{17}$$

Considering the Eqs. 5, 16 and 17 one can formulate the corresponding inhomogeneous Helmholtz-differential equation

$$\beta\,\mathrm{div}\,\mathrm{grad}\,\kappa-\alpha\,\kappa=\frac{1}{2}(\mu_{\mathrm{I}}-\mu_{\mathrm{B}})(\mathrm{I}_{\mathbf{B}}-3)+\sum_{j=1}^{n}\frac{1}{2}\left(\mu^{j}_{\mathrm{I}}-\mu^{j}_{\mathrm{B}}\right)(\mathrm{I}_{\mathbf{B}^{j}_{e}}-3). \tag{18}$$

In the opinion of the authors it is not possible to derive an analytical solution for the coupled finite viscoelastic problem, but we investigated the corresponding 1-dimensional differential equation of the structure parameter arising in the simple shear problem. This study results in a solution of the correspondent homogeneous equation which is the sum of two exponential functions and an additive inhomogeneous solution. The latter is damped by the identified parameters as usual for an equation which has got the form of a "phase transition problem". The boundary conditions for κ are assumed to be 1 near the substrate. That means that we only have interphase material at this part of the bonds. The opposite value, $\kappa=0$, stands for the bulk

material. Hence the additional model parameters α and β adjust the field function $\kappa(\mathbf{x}, t)$ which is responsible for the interpolation between bulk and interphase properties. There remains a dissipation inequality, from which n evolution equations are developed in accordance with the works of Sedlan [47] and Lion [46].

$$\dot{\mathbf{C}}_i^j = 2\left[(1-\kappa)\,\frac{1}{r_\mathrm{B}}^j + \kappa\frac{1}{r_\mathrm{I}}^j\right] * \left[\mathbf{C} - \frac{1}{3}\mathrm{tr}(\mathbf{C}\cdot\mathbf{C}_i^{j-1})\mathbf{C}_i^j\right]. \tag{19}$$

In these equations, there are n relaxation times for each bulk phase r_B^j and interphase r_I^j. The resulting tensor $\mathbf{C}$ is the right Cauchy-Green deformation tensor, whereas the tensors $\dot{\mathbf{C}}_i^j$ are the time-dependent variations of the inelastic right Cauchy-Green deformation tensors $\mathbf{C}_i^j$. The evolution equations again reflect the split into two phases and the structure parameter allows for an interpolation between the two. A number of material parameters were introduced, which will be strategically determined in the course of this work, namely: $\mu_\mathrm{B}, \mu_\mathrm{I}, \mu_\mathrm{B}^j, \mu_\mathrm{I}^j, \alpha, \beta, r_\mathrm{B}^j, r_\mathrm{I}^j, (j = 1, \ldots, n)$.

Identification of parameters and simulation

Identifying the parameters is an inverse problem. The material parameters must be determined under the condition that the simulation results match the data obtained in the real experiments. For solving this inverse problem, a target function is set in the form of a quality criterion that reflects the match between simulation and experiment. This target function is formulated as the sum of residual errors between simulation and experiment and is minimised by incrementally changing the material parameters. For an optimum set of parameters, this sum must be zero.

We chose a gradient-free optimisation method [68, 69] for the computer-aided optimisation (CAO). Beginning with a chosen starting vector (parent vector), an iterative algorithm based upon evolution strategies is used to find the optimum set of parameters. A random number generator (Monte Carlo algorithm) generates several new vectors (child vectors) by modifying the parent vector [70]. In the next step, the boundary value problem (BVP) is analysed for the different child vectors. The vectors that best meet the quality criterion are chosen as parents for the next generation. The advantage of this algorithm is its robustness, as it needs only the target function and not its gradient. As opposed to gradient-based methods, it is furthermore less probable to converge into local minima and can be used as *Black Box* for the most diverse classes of problems and material models without having to calculate sensitivities. Evolution strategy-based calculations are more time-consuming, though, but can easily be parallelised on a PC cluster.

The strategy used for parameter identification is as follows: First, the basic elasticity material parameters for bulk phase μ_B and interphase μ_I are determined for the thickest (bulk phase with $\kappa = 0$ assumed in the entire volume) and for the thinnest (interphase with $\kappa = 1$ assumed in the entire volume) bonds. The shear moduli are taken from the stress/shear graph. In our case, these moduli are $\mu_\mathrm{B} = 1.70$ MPa for the bulk phase and $\mu_\mathrm{I} = 0.6$ MPa for the interphase.

Second, the viscoelastic parameters have to be determined by analysing the thickest bonds in this respect. Two Maxwell elements prove to be sufficient to adequately represent the viscoelastic behaviour of the shear sample in the examined range of shear rates (0.004 and 0.04 s^{-1}).

The relaxation spectrum is split into decades [17], whereby two decades, which are represented by two Maxwell elements, are activated.

The displacement exerted on the samples by the RS5 machine is measured as a function of time and included as a time-dependent boundary condition in the parameter identification process.

As the problem itself is homogenous, it suffices to consider one single point of the corresponding displacement-driven boundary value problem to identify the parameters.

Figure 11 shows a good match between experimental data and simulation data. The parameters identified for the Maxwell elements are $\mu_\mathrm{B}^1 = 1.949\,\mathrm{MPa}, \mu_\mathrm{B}^2 = 0.417\,\mathrm{MPa}, r_\mathrm{B}^1 = 2.883\,\mathrm{s}, r_\mathrm{B}^2 = 92.556\,\mathrm{s}$.

Third, the same procedure is applied to the sample with the thinnest bond to determine the viscoelastic behaviour of the interphase or boundary layer. Here, too, a homogenous problem is solved for two Maxwell elements. The displacement boundary condition for this sample is almost linear in time, as can be seen from the stress/shear response (Fig. 12). This is due to the fact that thin bonds are far less stiff than thick bonds, thus opposing less resistance to the RS5 machine.

Figure 12 also shows an excellent match between simulation and experimental data. The parameters identified for the Maxwell elements are $\mu_\mathrm{I}^1 = 0.295\,\mathrm{MPa}, \mu_\mathrm{I}^2 = 0.089\,\mathrm{MPa}, r_\mathrm{I}^1 = 2.894\,\mathrm{s}, r_\mathrm{I}^2 = 92.296\,\mathrm{s}$. When comparing the viscoelasticity parameter sets of the bulk phase and the interphase, one can interestingly observe that the relaxation times are independent of the bond thicknesses. The viscoelastic behaviour differs only in stiffnesses/shear moduli of the springs in the Maxwell elements.

In order to optimize the model parameters α and β in the extended model, an inhomogenous boundary value problem is solved in a finite element calculation as part of a multi-field problem. During identification it turned out that the solution for the structure parameter depends only on the relation between α and β. For this reason we set $\beta = 1.0$ N,

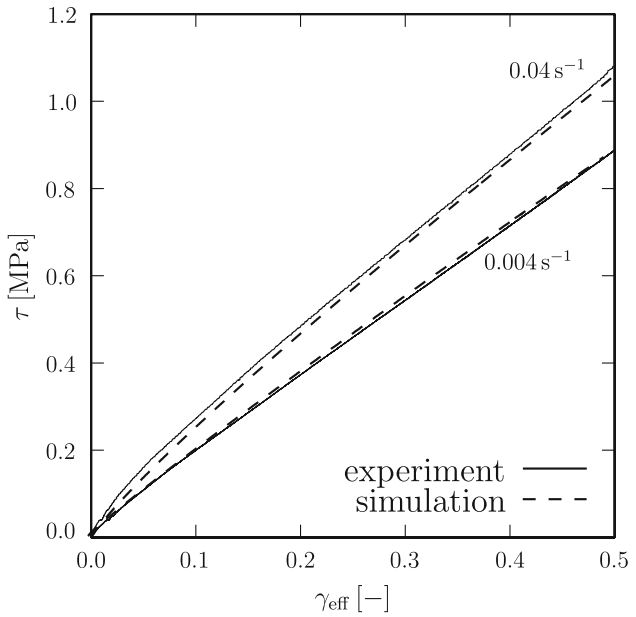

Fig. 11 Comparison of simulation and experimental data for thick bonds (here 2,206 μm) sheared at rates of 0.004 s^{-1} and 0.04 s^{-1}

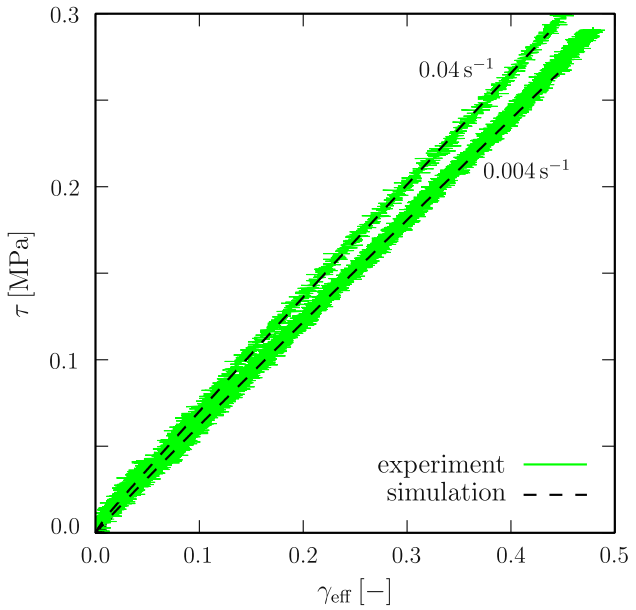

Fig. 12 Comparison of simulation and experimental data for thin bonds (here 86 μm) sheared at rates of 0.004 s^{-1} and 0.04 s^{-1}

leaving the problem to be solved consistent in its physical units. Parameter α was identified as 657.0 MPa. When comparing the basic elasticity experimental data to the simulation results of the extended model in Fig. 13, one can see that, with the exception of the range below 100 μm, the simulation matches the experimental data very well. Considering the relatively high standard deviation of the experimental data in the above-mentioned range, the overall result must be rated as exceptionally good.

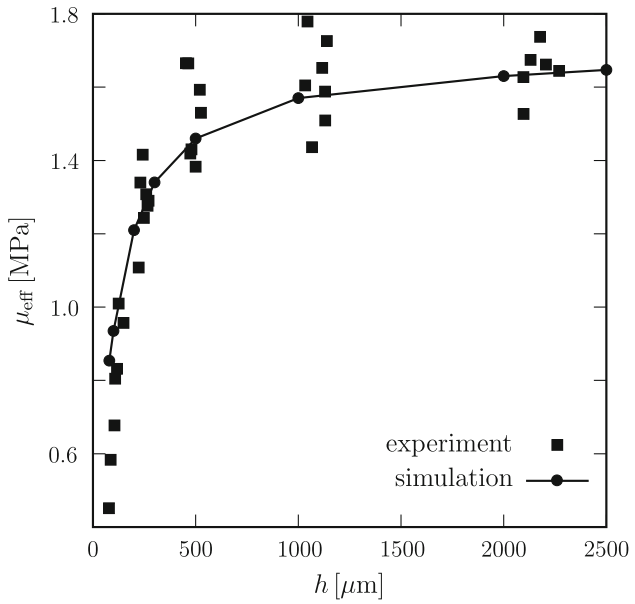

Fig. 13 Comparison of simulation and experimental data: effective shear modulus μ_{eff} [MPa] as a function of bond thickness h [μm] for basic elasticity

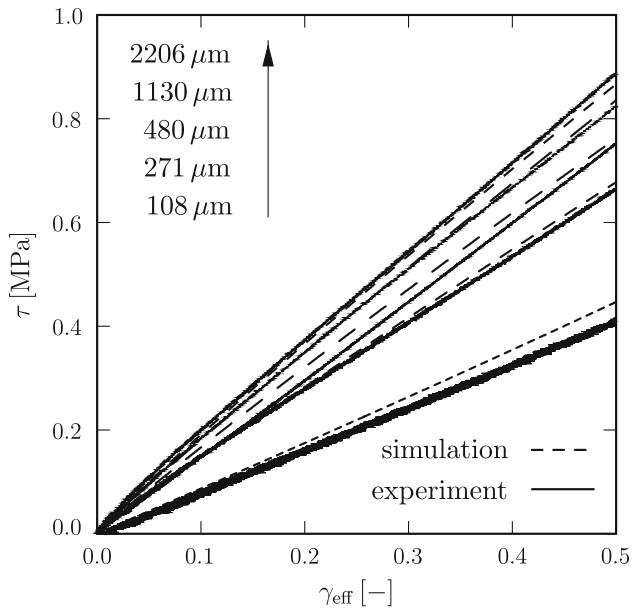

Fig. 14 Comparison of the experimental viscoelastic data set with the simulation of the extended model for a shear rate of 0.004 s^{-1} and bond thicknesses of 108–2,206 μm

In a final step, shear tests with bond thicknesses taken from the actual samples and ranging from 108 to 2,206 μm are simulated with shear rates between 0.004 and 0.04 s^{-1} to assess the identified parameters of the extended model. The simulation results are shown in Figs. 14 and 15. Again the simulation matches the experimental data very well. Hence no further adjustment of the parameters was deemed

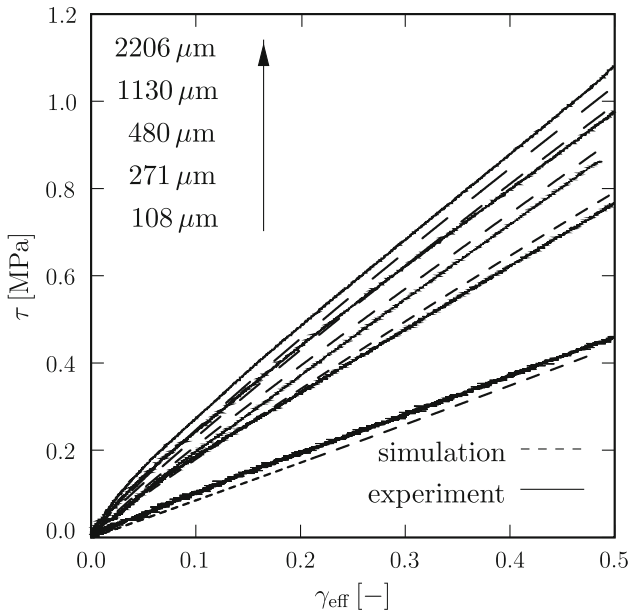

Fig. 15 Comparison of the experimental viscoelastic data set with the simulation of the extended model for a shear rate of 0.04 s^{-1} and bond thicknesses of 108–2,206 μm

necessary, which would have taken a long time due to the numerous inhomogenous boundary problems.

Conclusion and outlook

In this study we are covering many disciplines of mechanics. Starting with a detailed description of our sample preparation, we subsequently provide an in-depth analysis of the entire experimental setup as well as of all experimental procedures performed.

The results obtained from shear-testing bonds with different thicknesses clearly show a pronounced size effect of the kind "thinner equals softer". This effect appears in both basic elasticity and viscoelasticity. On the theoretical side, a new extended continuum mechanics-based material model is presented, which is thermomechanically consistent and able to represent the phenomena observed during the experiments. The introduced model parameters are determined by means of an evolution strategy. The comparison between simulation and experimental data shows a very good correlation for the extended model. Future experiments will examine polyurethane bonds on different substrates and surfaces. Furthermore, the triol/diol mixture ratio will be varied to systematically modify the polyurethane's mechanical properties, with the aim of really putting this extended model to the test. Another important step will be the inclusion of thermomechanical effects. Currently temperature-controlled shear samples are being developed to research into the range of the glass transition temperature and gain more information about the formation of the interphases or boundary layers. This will require a thermomechanical coupling to be added to the model presented here. Nevertheless, we cannot give any physical interpretation for the formation of the boundary layer and the resulting effect "thinner equals softer" at the moment. Even specialists in this domain are not able to give detailed information about the processes in the bonds near the substrates during the hardening process. So it is our aim to continue the project so that we can deal with this phenomenon.

Acknowledgements The authors are grateful to the DFG (Deutsche Forschungsgemeinschaft—German Research Foundation) for financial support under grant numbers Di 430/5-1 to 5-3 and Po 577/15-1.

References

1. Bockenheimer C, Valeske B, Possart W (2002) Int J Adhes Adhes 22:349
2. Fata D, Bockenheimer C, Possart W (2005) In: Possart W (ed) Adhesion-current research and applications. Wiley-VCH, Weinheim, p 479
3. Krüger JK, Possart W, Bactavachalou R, Müller U, Britz T, Santuary R, Alnot P (2004) J Adhesion 80:585
4. Chung J, Munz M, Sturm H (2005) J Adhesion Sci Technol 19:1263
5. Possart W, Krüger JK, Wehlack C, Müller U, Petersen C, Bactavatchalou R, Meiser A (2004) C R Chimie 9:60
6. Bouchet J, Roche AA (2002) J Adhesion 78:799
7. Roche AA, Bouchet J, Bentadjine S (2002) Int J Adhes Adhes 22:431
8. Bouchet J, Roche AA, Jacquelin E (2002) J Adhesion Sci Technol 16:1603
9. Bouchet J, Roche AA, Hamelin P (2002) Thin Solid Films 355:270
10. Vanlandingham MR, Dagastine RR, Eduljee RF, McCullough RL, Gillespie JW Jr (1999) Compos Part A: Appl Sci Manuf 30:75
11. Wehlack C, Possart W, Krüger JK, Müller U (2007) Soft Mater 5:87
12. Schlimmer M, Hennemann OD, Hahn O (2004) AiF project 76
13. Schlimmer M, Bornemann J (2004) Berechnung und Dimensionierung von Klebverbindungen mit der Methode der Finiten Elemente und experimentelle Überprüfung der Ergebnisse. Forschungsbericht 1-2003, Schriftenreihe des Instituts für Werkstofftechnik der Universität Kassel, Kassel
14. Schlimmer M, Hahn O, Hennemann OD (2006) Methodenentwicklung zur Berechnung und Auslegung geklebter Stahlbauteile im Fahrzeugbau bei schwingender Beanspruchung. Proc Gemeinsame Forschung in der Klebtechnik-6. Kolloquium 21./22. Februar
15. Diebels S, Johlitz M, Steeb H, Batal J, Possart W (2007) J Phys: Conf Ser 62:34
16. Johlitz M, Steeb H, Diebels S, Batal J, Possart W (2007) Technische Mechanik, accepted
17. Johlitz M, Steeb H, Diebels S, Chatzouridou A, Batal J, Possart W (2007) J Mat Sci 42:9894
18. Steeb H, Diebels S (2004) Int J Solids Struct 41:5071
19. Goodman M, Cowin S (1972) Arch Rat Mech Anal 44(4):249
20. Helm D (2001) Formgedächtnislegierungen (Bericht-Nr. 3/2001 des Instituts für Mechanik, Kassel

21. Helm D (20077) Int J Numer Meth Eng 69:1997
22. Capriz G, Podio-Guidugli P, Williams W (1982) Meccanica 17:80
23. Capriz G (1980) Continua with microstructures. Springer, New York
24. Svendsen B (1999) Continuum Mech Therm 4:247
25. Svendsen B, Hutter K, Laloui L (1999) Continuum Mech Therm 4:263
26. Coleman B, Noll W (1963) Arch Rat Mech Anal 13:167
27. Coleman B, Gurtin ME (1967) J Chem Phys 47:597
28. Chadwick P (1974) Phil Trans Roy Soc Lond A 276:371
29. Alts T (1979) Prog Coll Pol Sci S 66:7367
30. Haupt P, Lion A, Backhaus E (2000) Int J Solids Struct 37:3633
31. Haupt P, Lion A (2001) A generalisation of the Mooney-Rivlin model to finite linear viscoelasticity Constitutive Models for Rubber. Swets & Zeitlinger, London
32. Haupt P, Lion A (2002) Acta Mech 159:87
33. Göktepe S, Miehe C (2005) J Mech Phys Solids 53:2259
34. Miehe C, Keck J (2000) J Mech Phys Solids 48:323
35. Miehe C, Göktepe S, Lulei F (2004) J Mech Phys Solids 52:2617
36. Miehe C, Göktepe S (2005) J Mech Phys Solids 53:2231
37. Keck J (1998) Zur Beschreibung finiter Deformationen von Polymeren, Experimente, Modellbildung, Parameteridentifikation und Finite-Elemente-Formulierung. Bericht-Nr. I-5 des Instituts für Mechanik (Bauwesen), Stuttgart
38. Reese S (2001) Thermomechanische Modellierung gummiartiger Polymerstrukturen. F01/4 Institut für Baumechanik und Numerische Mechanik, Hannover
39. Reese S, Govindjee S (1998) Mech Time-Depend Mater 1:357
40. Reese S, Govindjee S (1998) Int J Solids Struct 35:3455
41. Reese S, Wriggers P (1997) Comput Methods Appl Mech Eng 148:279
42. Reese S, Wriggers P (1999) Modelling of the thermomechanical material behaviour of rubber-like polymers-micromechanical motivation and numerical simulation (Dorfmann & Muhr (eds) Rotterdam, 1999), p 13
43. Lion A (1996) Continuum Mech Therm 8:153
44. Lion A (1997) Acta Mech 123:1
45. Lion A (1999) Rubber Chem Technol 72:410
46. Lion A (2000) Thermomechanik von Elastomeren. Bericht-Nr. 1/2000 des Instituts für Mechanik, Kassel
47. Sedlan K (2001) Viskoelastisches Materialverhalten von Elastomerwerkstoffen, Experimentelle Untersuchung und Modellbildung. Berichte des Instituts für Mechanik (2/2001), Universität Gesamthochschule Kassel, Kassel
48. Amin AFMS, Alam MS, Okui Y (2002) Mech Mater 34:75
49. Amin AFMS, Alam MS, Okui Y (2003) J Test Eval 31(6):524
50. Amin AFMS, Lion A, Sekita S, Okui Y (2006) Int J Plasticity 22:1610
51. Laiarinandrasana L, Piques R, Robisson A (2003) Int J Plasticity 19:977
52. Bergstrom JS, Boyce MC (1998) J Mech Phys Solids 56(5):931
53. Boyce MC, Arruda EM (2000) Rubber Chem Technol 73:504
54. Bergstrom JS, Boyce MC (2001) Macromolecules 34(3):614
55. Bergstrom JS, Boyce MC (2001) Mech Mater 33:523
56. Bergstrom JS, Boyce MC (2000) Mech Mater 32:627
57. Besdo D (2003) Int J Plast 19:1001
58. Besdo D (2003) Int J Plast 19:1019
59. Ihlemann J (2002) Kontinuumsmechanische Nachbildung hochbelasteter technischer Gummiwerkstoffe. Institut für Mechanik (Maschinenbau) Universität Hannover, Hannover
60. Lubliner J (1985) Mech Res Commun 12:93
61. Tallec PL, Kaiss A, Rahier C (1994) Int J Numer Meth Eng 37:1159
62. Kröner E (1960) Arch Ration Mech Anal 4:273
63. Lee EH, Liu DT (1967) J Appl Phys 38:19
64. Lee EH (1969) J Appl Mech 36:1
65. Mooney M (1940) J Appl Phys 11:582
66. Rivlin RS (1948) Phil Trans Roy Soc Lond A 241:379
67. Cahn JW, Hilliard J (1958) J Chem Phys 28:258
68. Scheday G (2003) Theorie und Numerik der Parameteridentifikation von Materialmodellen der finiten Elastizität und Inelastizität auf der Grundlage optischer Feldmessmethoden. Bericht-Nr. I-11 des Instituts für Mechanik (Bauwesen), Stuttgart
69. Schwefel HP (1995) Evolution and Optimum Seeking. Wiley, New York
70. Rechenberg I (1973) Evolutionsstrategie: optimierung technischer Systeme nach Prinzipien der biologischen Evolution. Frommann-Holzboog, Stuttgart